Mixed Brownian alignment and Néel rotations in superparamagnetic iron oxide nanoparticle suspensions driven by an ac field

Saqlain A. Shah, Daniel B. Reeves, R. Matthew Ferguson, John B. Weaver, and Kannan M. Krishnan

Phys. Rev. B **92**, 094438 — Published 24 September 2015

DOI: 10.1103/PhysRevB.92.094438

Mixed Brownian alignment and Néel rotations in superparamagnetic iron-oxide nanoparticle suspensions driven by an AC field

Saqlain A Shah,[1,2] Daniel B Reeves,[3] R Matthew Ferguson,[4,1] John B Weaver,[3,5] and Kannan M Krishnan[1,a)]

[1)] *Materials Science and Engineering, University of Washington, Seattle, WA 98195 USA*

[2)] *Dept. of Physics, Forman Christian College (University) Lahore, Pakistan*

[3)] *Dept. of Physics and Astronomy, Dartmouth College, Hanover NH 03755 USA*

[4)] *LodeSpin Labs, PO Box 95632, Seattle, WA 98145 USA*

[5)] *Dept. of Radiology, Geisel School of Medicine, Hanover NH 03755 USA*

(Dated: 14 September 2015)

Superparamagnetic iron oxide nanoparticles with highly nonlinear magnetic behavior are attractive for biomedical applications like magnetic particle imaging and magnetic fluid hyperthermia. Such particles display interesting magnetic properties in alternating magnetic fields and here we document experiments that show differences between the magnetization dynamics of certain particles in frozen and melted states. This effect goes beyond the small temperature difference ($\Delta T \sim 20^{\circ}C$) and we show the dynamics to be a mixture of Brownian alignment of the particles and Néel rotation of their moments occurring in liquid particle suspensions. These phenomena can be modeled in a stochastic differential equation approach by postulating log-normal distributions and partial Brownian alignment of an effective anisotropy axis. We emphasize that precise particle-specific characterization through experiments and nonlinear simulations is necessary to predict dynamics in solution and optimize their behavior for emerging biomedical applications including magnetic particle imaging.

[a)] Electronic mail: kannanmk@uw.edu

I. INTRODUCTION

Superparamagnetic iron oxide nanoparticles (SPIOs) made of magnetite can possess magnetic moments that saturate in biologically relevant magnetic fields of the order of tens of mT. This strong magnetization response allows non-invasive control and readout during biomedical applications. Because SPIOs are biocompatible, they have been extensively used to realize drug delivery, cell separation, magnetic resonance imaging (MRI), localized hyperthermia therapy[1] and, most recently, magnetic particle imaging (MPI)[2], which exploits the nonlinear response of magnetic nanoparticles to oscillating magnetic fields as a signal. In MPI and most biomedical applications (separation being a notable exception) the particles are activated with an alternating magnetic field, and thus magnetization reversal dynamics play a critical role[3–8]. There are two possible rotation mechanisms: Néel rotation[9] governs the restructuring of electronic spin states to allow the magnetic moment to reorient irrespective of the orientation of the whole particle, and Brownian rotation[10] occurs when the particle itself rotates in the solution, carrying with it the magnetic moment fixed in direction relative to the particle's crystal lattice. As an illustrative instance of why both mechanisms are important, hyperthermia therapy usually relies on Néel rotations that locally heat when the response of the moment lags behind the driving field, yet several studies now show the influence of particle alignment or orientations on the heating capabilities, indicating Brownian rotations may be useful, if not inherently used as a mechanism of heating.[11–13]

In this paper, combining experiments and modeling, we have uncovered interesting solution-phase dependent magnetic dynamics through rigorous testing of magnetization responses in various frozen and melted configurations. For example, we observed a change in magnetic response of a dilute suspension of particles to an alternating field upon freezing, which reversed upon melting. We attribute differences between the liquid and frozen responses to the additional (Brownian) rotational freedom of the particles. To be clear, we assume that in the liquid suspension, the particles can reorient their easy axes to align with the applied field, and this Brownian rotation is not possible in the frozen state. When a static magnetic field was applied concurrently with the freezing process, possibly imparting a net alignment of the easy axes, further variation in magnetic behavior was observed. The basic idea of the title phrase "Brownian alignment and Néel rotation" is shown in Fig. 1: 1) the entire crystal rotates slightly to align one of its easy axes and 2) the subsequent

magnetization rotation with the Néel mechanism is different than the unaligned case.

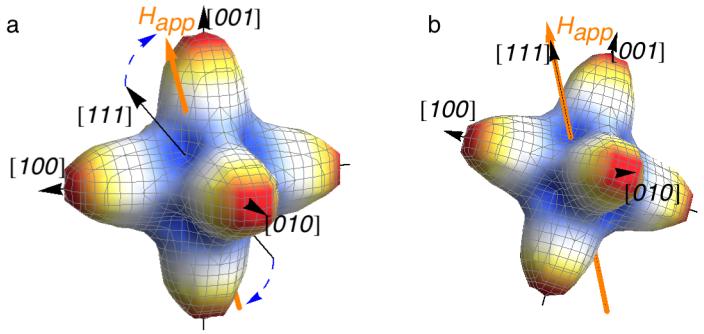

FIG. 1. The magnetocrystalline energy surface for cubic magnetite (negative K1), which has easy directions in the [111] family. After applying an arbitrary magnetic field vector H_{app} in a fixed direction as in (a), particles in solution undergo Brownian rotation through a small angle until as in (b) the nearest easy axis is aligned with the applied field.

We compare these results to nonlinear stochastic simulations and find the behaviors can be replicated when the direction of the effective easy axis is no longer random, but is partially aligned in the field. From these observations, we conclude that the relative rotational freedom of nanoparticles, and the orientation of easy axes with respect to an applied field can have a significant impact on the response to an oscillating field even when the Néel reversal process dominates. This can impact biomedical applications such as magnetic particle imaging or magnetic fluid hyperthermia.

II. EXPERIMENTAL MATERIALS AND METHODS

A. Materials characterization

Magnetite nanoparticles (sample LS-002-2) were obtained from LodeSpin Labs, LLC. The nanoparticles contained crystalline magnetite cores that were coated with a PEG-based amphiphyllic polymer. Sample LS-002-2 was coated with poly(maleic anhydride alt-1 octadecene) (PMAO, Mn 40,000 Dalton) -poly(ethylene glycol) (PEG, Mn 20,000 Dalton). The PMAO was loaded with PEG such that 25% of the available carboxylates in the PMAO were bonded to a PEG molecule. For this study, sample LS-002-2 was dispersed in dimethyl sulfoxide (DMSO), which freezes at 19 °C. The hydrodynamic diameter (Z-average, i.e. the

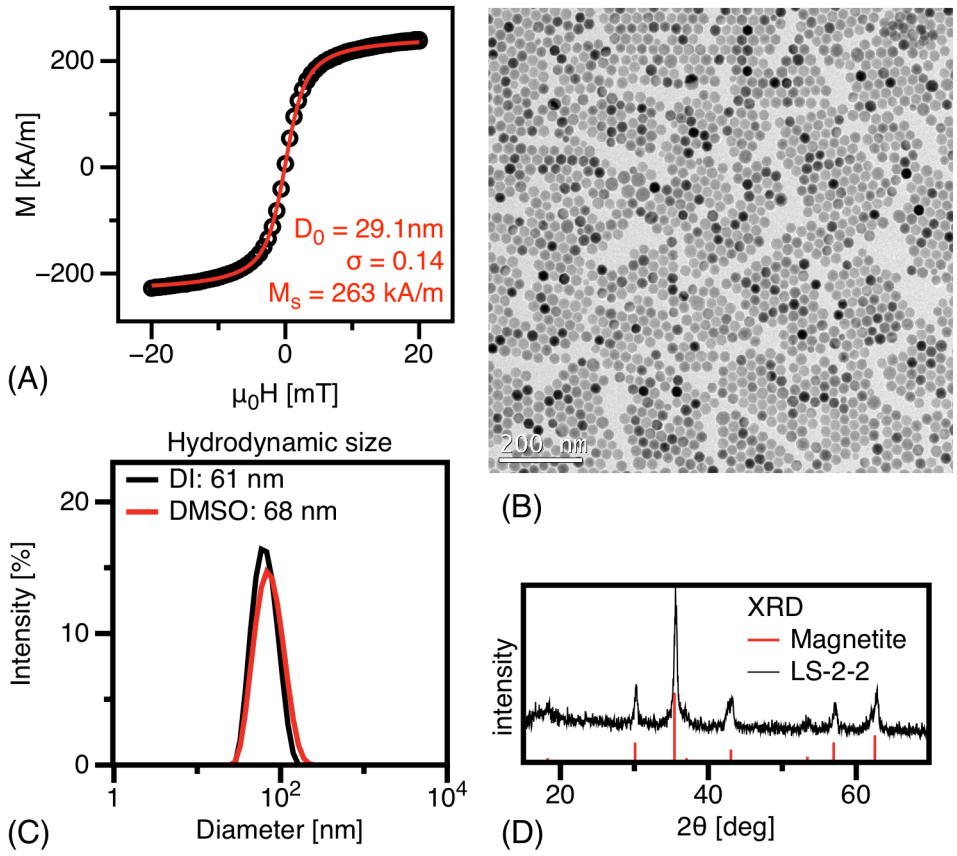

FIG. 2. SPIOs were characterized by complementary methods to obtain magnetic, size, and structural information: (A) Vibrating sample magnetometer (VSM) curve, (B) Transmission electron microscope (TEM) image of nanoparticles showing monodisperse size distribution, (C) Dynamic light scattering (DLS) plot and (D) X-ray diffraction plot

intensity based harmonic mean) of nanoparticles in liquid DMSO was 68 ± 25 nm, measured by Dynamic Light Scattering (DLS). The diameter of the same sample dispersed in water was 61 ± 20 nm.

Magnetic performance was the same in DMSO and water which have similar viscosities (for reference, the viscosity of DMSO is 1.996 cP, while water is 0.894 cP). Transmission electron microscopy (TEM) images in Fig. 2 showed the nanoparticle samples to be monodisperse, with median diameter of 26 ± 1.5 nm. Multiple images (6000 particles) were analyzed to determine size distribution using ImageJ, an open source image processing software developed by the National Institutes of Health. Shape anisotropy of the particles was estimated from TEM images, also using ImageJ. Each particle measured for size-determination was

fit with an ellipse and the ratio of long axis to the short axis determined. The resulting histogram was fit with a log-normal distribution to determine the median aspect ratio (1.04 ± 0.03). This equates to a typical elongation of approximately 1nm. Fig. 2 also shows the vibrating sample magnetometer (VSM) curve and the log-normal size distribution of nanoparticles obtained by fitting the magnetization curve to the Langevin function using Chantrell's method[14]. We calculate that the median magnetic core diameter is 29.1 ± 1.5 nm, with $\sigma_{nw} = 0.05$ (number-weighted), where $\exp(\sigma_{nw})$ is the geometric standard deviation of the log-normal distribution. The measured saturation magnetization of 263 kA/m was used for fitting to determine the magnetic size from VSM measurements. Powder x-ray diffraction patterns matched a magnetite reference (Figure 1D), although we note the saturation magnetization was about 57% of bulk magnetite, which may be due to some phase impurity. Magnetite is ferrimagnetic having an inverse spinel crystalline structure and displays a cubic magnetocrystalline anisotropy, with easy axes along the [111] directions, i.e. the body diagonals of a cube. The angles between the eight equivalent easy axes in a perfect cube are 70.53°.

B. Immobilization of SPIOs

Sample SPIOs were suspended in DMSO and immobilized by freezing in the absence or presence of a static magnetic field. To prepare samples, a solution containing 200 μL of MNPs with concentration 1.22 gFe/L was transferred to 0.6 mL micro-centrifuge tube and sonicated for five minutes at room temperature (23 °C). After sonication, the DMSO solution was visibly in the liquid phase. The sample was immobilized by freezing at -20 °C inside a commercial freezer. During freezing, a magnetic field was applied to the sample to orient the nanoparticles by aligning their magnetic easy axes. The magnetic field was arranged with field lines parallel, transverse, or diagonal to the reference axis, defined to be along the axis of the sample tube (see Fig. 3). The magnetic field was generated by a NdFeB permanent magnet (K&J magnetics, Grade N42; Dimensions: 1.5 × 1 × 0.125 inches). The liquid sample was frozen in three different magnetic fields (5, 10, and 15 mT) with a zero field control sample, and for the three respective orientations. For each freezing condition, the sample was cooled to -20 °C under the applied field and kept at that temperature for 30 minutes. After freezing, the sample tube was transferred to an ice-bath (0 °C) to maintain

the frozen state of the ferrofluid during magnetic particle spectroscopy (MPS) measurements. Repeated MPS measurements showed that the freezing process was fully reversible and the sample behavior upon melting was the same as before freezing. In another study, a dilution series (0.05, 0.1, 0.5, 1, 1.22 gFe/L) was prepared and analyzed with the same measurement procedure after freezing in different fields (0, 10, 60 mT) to determine whether the freezing process introduced inter-particle interactions into the magnetic behavior of the system.

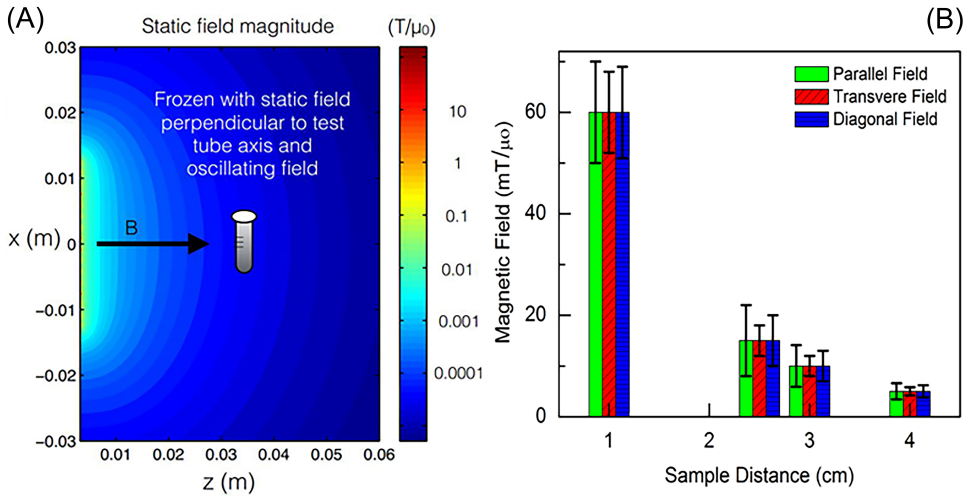

FIG. 3. (A) The simulated magnetic field of the permanent magnet (lines of equal field strength are shown in the figure). The test tube containing the SPIOs was frozen in this orientation at various distances to achieve the varying magnetic field amplitudes. In the example illustrated in (A), the aligning field was applied perpendicular to the direction of the oscillating (drive) field, which was always applied parallel to the long axis of the sample tube. The surface field for these magnets is 0.12 T, so we see that at 5 cm the field is in the single mT range as shown in experiment. Notably at this distance we can see the variations in the field are minimal within the test tube. (B) Measured variation of field strength with distance from the magnet. Error bars represent the variation in field within the sample tube for the stated field orientation, and differ because the tube geometry is anisotropic.

The magnetic field profile of the NdFeB magnet was measured using a handheld gaussmeter (Lakeshore model 410). Distance was measured from the center of the magnet to the center of the sample volume. Uncertainties in the magnetic field profile, represented by error bars in Fig. 3(b), were estimated based on the range of field values measured over the sample volume along the magnetic field vector (maximum 1.4 cm, for the parallel orientation). The

largest field corresponded to the volume of sample closest to the magnet, and the smallest field to the volume furthest from the magnet. The parallel orientation admitted the largest uncertainty, as the sample volume was longest in this direction.

C. Magnetic measurements

A custom-built magnetic particle spectrometer was used to determine the magnetization response of MNPs[3,15]. The system applies an oscillating magnetic field to the sample of MNPs and measures the voltage signal induced in a receiver coil from the response of the magnetic particles. The signal is thus the time derivative of the magnetization and must be integrated numerically to obtain the magnetization response.

D. LLG simulations with effective anisotropy

Simulations of magnetization reversal were incorporated to support experiments. There have been many models introduced in the literature to model the rotational dynamics of magnetic particles[16–19]. Here, state of the art simulations integrate the stochastic Landau-Lifshitz-Gilbert (LLG) equation Eq. 1. The equation describes a classical magnetic dipole with a phenomenological damping term and can be used to discuss Néel rotations of magnetic particles[16,20]:

$$\frac{\mathrm{d}\mathbf{m}}{\mathrm{d}t} = -\frac{\gamma}{1+\alpha^2}\left\{\mathbf{m}\times\left[\mathbf{H}+\alpha\mathbf{m}\times\mathbf{H}\right]\right\}. \tag{1}$$

In the LLG dynamics, the magnetization $\mathbf{m}$ evolves over time depending on the gyromagnetic ratio γ and the unitless LLG damping parameter α. To model magnetic spectroscopy of SPIOs with core volume V_c and magnetic moment μ, we considered the total field $\mathbf{H}$ to contain contributions from an applied oscillating excitation field of magnitude H_0 and frequency $f = \omega/2\pi$, an effective uniaxial anisotropy direction with magnitude K and easy axis in direction $\mathbf{n}$. Particles in liquid suspension are not fixed spatially and undergo Brownian motion; in all samples the concentration of nanoparticles was on the order of 1 g/L, making the volume fraction of particles 0.025%. For both of these reasons we modeled the particles as non-interacting dipoles. We could thus ignore translational movement in the model. However, it was essential to introduce thermal fluctuations of the direction of the

magnetization using a random field $\mathbf{h}(t)$ so that the total field of the model was

$$\mathbf{H} = H_0 \cos(\omega t)\, \hat{z} + \frac{2KV_c}{\mu}(\mathbf{m}\cdot\mathbf{n})\mathbf{n} + \mathbf{h}(t), \tag{2}$$

with a zero mean, delta-time correlated random field

$$\langle \mathbf{h}(t) \rangle = 0 \quad \langle \mathbf{h}_i(t)\mathbf{h}_j(t') \rangle = \frac{2k_{\mathrm{B}}T}{\mu\gamma}\frac{(1+\alpha^2)}{\alpha}\delta_{ij}\delta(t-t') \tag{3}$$

so that the field is Markovian in time and $i, j \in x, y, z$ describe the lack of correlation between the random fields in different cartesian directions. The thermal energy $k_{\mathrm{B}}T$ is written in terms of Boltzmann's constant and temperature T.

The model assumes the particles are effectively single domain, which is a reasonable assumption given that the critical diameter for multiple-domains in magnetite is approximately 85 nm[21]. A distribution for the magnetic moments was determined from the measured saturation magnetization and the measured core size distribution. The anisotropy is of particular interest and because the underlying mechanism is not fully understood, we used an effective anisotropy distribution, that could incorporate crystalline anisotropy, and shape anisotropies potentially caused by minor chaining (e.g., dimerization). This approach was taken by Jamet *et al.* to discuss multiple anisotropic contributions in clustered nanoparticles and by Tamion *et al.* to numerically account for the distribution of anisotropy constants[22,23]. We expect that in solutions, the particles were rotating with the Brownian mechanism to align one of their cubic axes along the applied field. The required angle of rotation is small on average because there are several equivalent axes in a cubic magnetite particle, and any one could align along the applied field. To simulate this behavior, we made nonrandom choices for the direction of an effective easy axis of each particle. We stress that the strength of the anisotropy was also considered a log-normal distribution and that the alignment with the field was modeled as a distribution of the angle of each particle's easy axis dependent on the extent of the alignment. For example, in the freezing experiments, we imagine a single particle immersed in a static field potentially allowing one of its easy axes—geometrically, the closest—to rotate and align with the field. The ensemble of particles thus develops a distribution of alignments that are locked in place when the solution is subsequently frozen. The alignment then persisted during spectroscopy. Coupled differential equations describing the Brownian and Néel rotation can be found in the works of Shliomis and Stepanov[24] as well as in Coffey, Cregg, and Kalmykov[25] though because of the foggy nature of the anisotropy

in this work and the excellent fit of the experimental data with the current model, these approaches were not used.

E. Numerical implementation

We use the Heun scheme to integrate the stochastic differential equation. Excellent descriptions of numerical methods for stochastic problems can be found in Gardiner's "handbook"[26]. Heun's method converges in the sense of Stratonovich[27] and can be written in general for the change in magnetization as:

$$\mathrm{d}\mathbf{m} = f(\mathbf{m}, t)\mathrm{d}t + g(\mathbf{m}, t)\mathrm{d}\mathbf{W}. \tag{4}$$

Here the numerical integration scheme has predictor

$$\bar{\mathbf{m}}(t + \Delta t) = \mathbf{m}(t) + f(\mathbf{m}, t)\Delta t + g(\mathbf{m}, t)\Delta\mathbf{W} \tag{5}$$

and then the true value is

$$\mathbf{m}(t + \Delta t) = \mathbf{m}(t) + \frac{f(\mathbf{m}, t) + f(\bar{\mathbf{m}}, t + \Delta t)}{2}\Delta t + \frac{g(\mathbf{m}, t) + g(\bar{\mathbf{m}}, t + \Delta t)}{2}\Delta\mathbf{W} \tag{6}$$

where an increment of the Wiener process is defined by $\Delta\mathbf{W} = \sqrt{\Delta t}\mathbf{N}(0, 1)$ where $\mathbf{N}(0, 1)$ is a vector of Normal or Gaussian distributed random numbers each with mean zero and unit variance.

The predicted size distributions for particle diameters are log-normal (see Fig. 2)[14]. This means the probability of having a particle with a certain radius r can be modeled by:

$$p(r) = \frac{1}{\sqrt{2\pi}}\frac{1}{r\sigma_r}\exp\left[-\frac{\left\{\ln\left(\frac{r}{m_r}\sqrt{1+\frac{s_r^2}{m_r^2}}\right)\right\}^2}{2\sigma_r^2}\right] \tag{7}$$

with

$$\int_0^\infty p(r)dr = 1. \tag{8}$$

We have used that the mean and standard deviation of the distribution are m_r and s_r respectively, and the scale parameter $\sigma_r = \sqrt{\ln(1 + \frac{s_r^2}{m_r^2})}$. An equivalent log-normal distribution for the anisotropy constants allows for a mixture of effects, including crystalline anisotropy and chaining. Simulations were always performed at the correct temperature (implemented in the thermal field, Eq. 3) corresponding to the desired experimental procedure. The LLG

damping parameter was held constant at $\alpha = 1$. Changing this value did not change the dynamics but required more time steps. It is typical to choose the value between 0.01 and 1[18,28,29] though new studies are shedding light on the variation of this parameter during ferromagnetic resonance[30]. The integration required 2^{12} time steps and 10^5 nanoparticles, or equivalently 10^5 simultaneous integrations of the stochastic equation. We included a signal at the background frequency to mimic any feed through from the apparatus (at most 10% of the magnitude of the nanoparticle signals and usually below 5%). The magnetite density was 4.9 g/cm^3 and the saturation magnetization was found from experiment to be 50 emu/g or equivalently 263 kA/m. Below Fig. 2 the measurement techniques are discussed. We used the bulk value for the gyromagnetic ratio of 1.3 GHz/T as opposed to the single electron value[31]. The best fit to experimental data was achieved using a mean anisotropy constant of 3.4 kJ/m^3 with a 3 kJ/m^3 standard deviation, which is consistent with recent measurements of similar samples[32]. In a suspension of particles, the easy axis, $\mathbf{n}$, for each particle is typically assumed to be in a random direction. However, the experiments showed that by freezing the particles in a static field, their subsequent magnetic dynamics were different. Two possible physical mechanisms were considered: the Brownian alignment of the closest magnetocrystalline easy axes, or formation of short chains in the direction of the applied field. Either way, this would replace the cubic anisotropy of the particles by an effective uniaxial anisotropy. To simulate this behavior, we allowed that an effective single easy axis for each particle was partially aligned with the direction of the static field. This was implemented by choosing a random orientation for each particle, adding a vector in the direction of alignment, and then normalizing again. Three realizations of this procedure are shown in Fig. 4: a fully randomized sample, a sample that has been aligned 30% to the transverse direction of the oscillating field, and a sample that has been aligned 50% parallel to the direction of the oscillating field.

III. RESULTS

Freezing the sample altered its dynamic magnetization, as shown in Fig. 5, which compares the response of a single sample in liquid and frozen states. Measurements were taken for a drive field of $f = 26$ kHz and $H_0 = 50$ mT/μ_0. By convention, only half of the full period (forward scan) is shown in all plots of the differential susceptibility $\chi_{diff} = dm/dH$ vs.

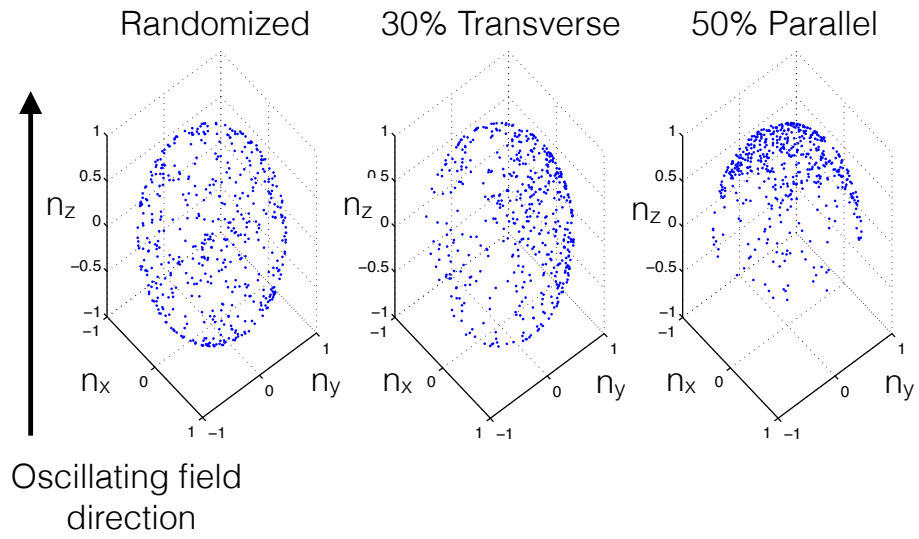

FIG. 4. Distribution of the effective easy axes of 500 particles. This figure should aid the visualization of the asymmetry that was included in the simulations in order to mimic partial alignment of an effective easy axis with the static field.

field with respect to the field amplitude. The fluid sample had greater maximum differential susceptibility $\chi_{diff}^{\max}$, and χ_{diff} decayed to its minimum at lower field magnitude.

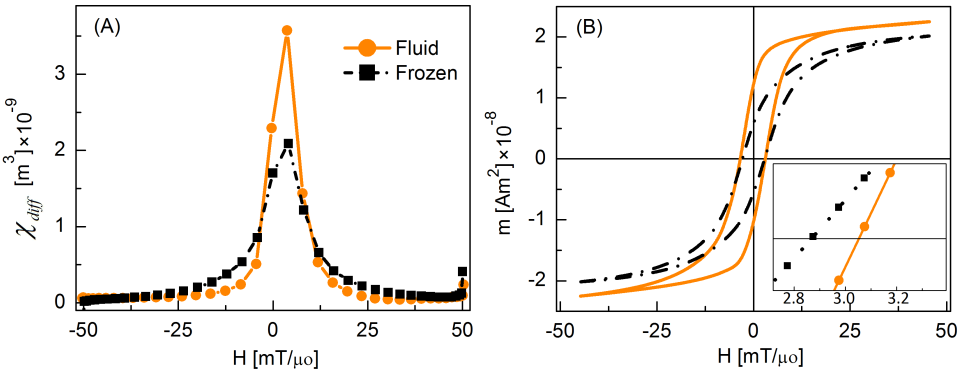

FIG. 5. MPS results of the same sample measured in fluid state (at 20 °C) and frozen (in zero magnetic field (0 mT/μ_0). The excitation field was 50 mT/μ_0 amplitude at 26 kHz (A) χ_{diff}, (B) $m(H)$ curves calculated by integrating data in (A).

When the sample was frozen in the presence of an applied field, both χ_{diff} and its

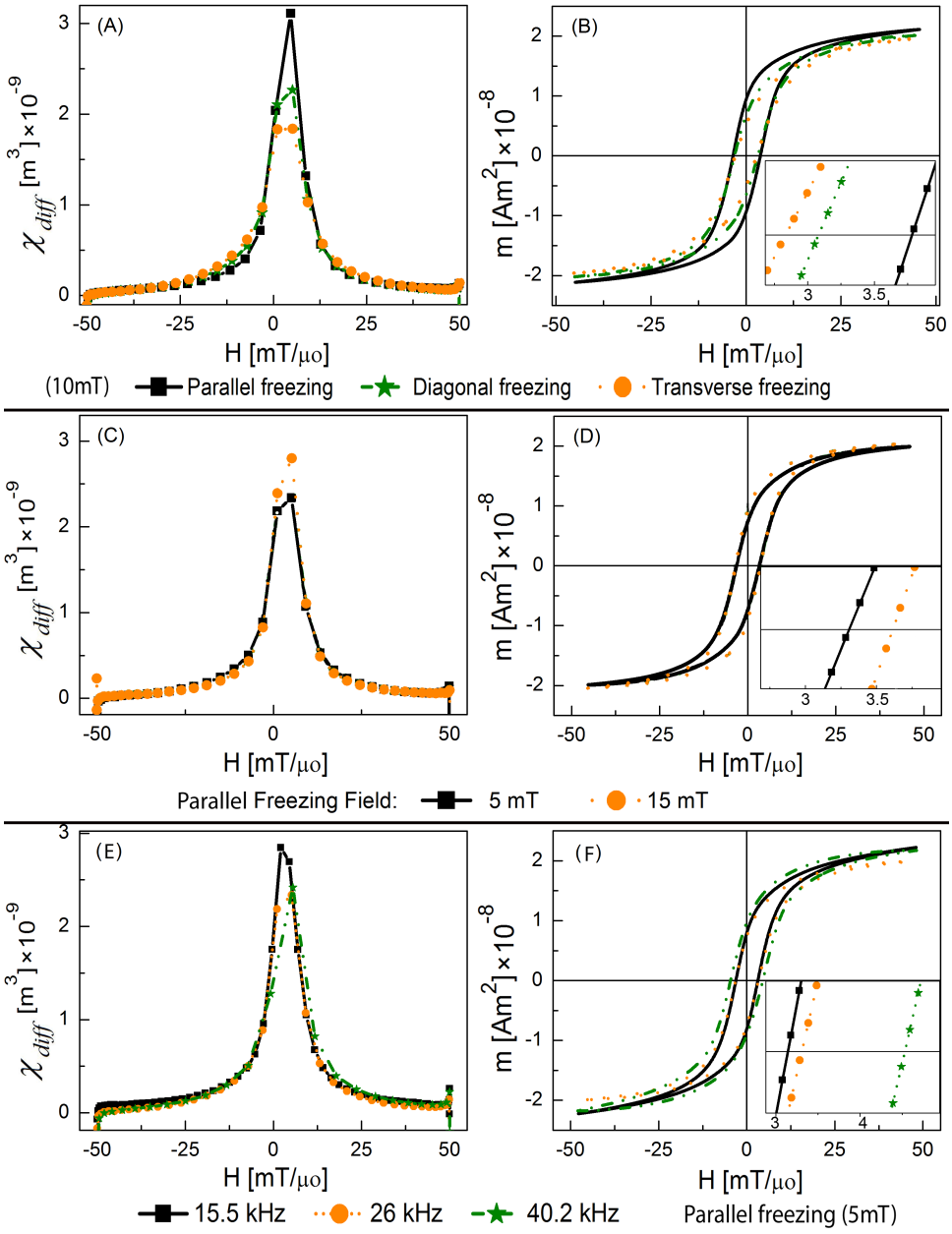

FIG. 6. MPS (26 kHz, 50 mT/μ_0) signal parameters of MNPs, field-frozen (10 mT/μ_0) along different directions with respect to the MPS applied field. (A) χ_{diff}, (B) integrated $m(H)$ curves. MPS (26 kHz, 50 mT/μ_0) signal parameters of MNPs, frozen in different magnetic fields along parallel orientation: (C) χ_{diff}, (D) $m(H)$ curves. MPS (50 mT/μ_0, different frequencies) signal parameters of MNPs, frozen in 5 mT/μ_0 along parallel orientation: (E) χ_{diff}, (F) $m(H)$ curves.

integrated value, the magnetization $m(H)$, varied with the angle of the applied field with respect to the reference axis (Fig. 6). Among the field-freezing data, the parallel orientation

had the highest value of $\chi_{diff}^{\max}$ (i.e. the maximum value of dm/dH [m^3], which is proportional to the maximum MPS signal intensity [V]) and highest coercivity, H_c. Freezing in the transverse orientation showed the minimum values of and H_c and the diagonal orientation showed intermediate values.

The magnetic response also varied with the intensity of the freezing field for a given angular orientation. Fig. 6C,D shows the magnetization response of MNPs frozen in different magnetic fields along parallel orientation. Among the field-freezing data, the smallest freezing-field led to the smallest values of $\chi_{diff}^{\max}$ and H_c. All these values increased with increasing freezing fields (Fig. 6), although the variation was relatively small, most probably due to the small range of freezing fields (15 mT/μ_0 maximum) that were achievable with our experimental apparatus. $\chi_{diff}^{\max}$ was the highest at 15 kHz and it decreased slightly as the frequency was increased. Coercivity H_c increased for increasing frequencies.

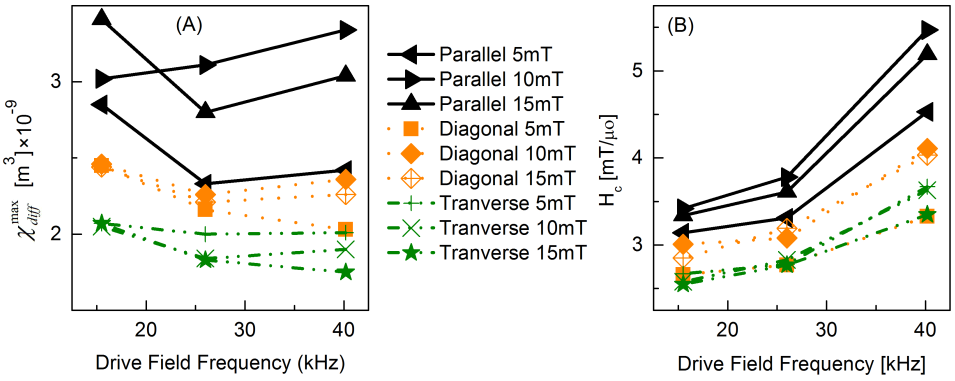

FIG. 7. Comparison plot of MNPs response for various combinations of freezing-fields, orientations and drive frequencies: (A) $\chi_{diff}^{\max}$, (B) Coercive field.

A summary of immobilized sample behavior is provided in Fig. 7, which plots variation of the peak value of the differential susceptibility $\chi_{diff}^{\max} = dm/dH$ and coercive field, H_c, for various combinations of freezing-fields, orientations and drive frequencies. Parallel-freezing gave the highest values for $\chi_{diff}^{\max}$ as well as H_c, whereas transverse freezing showed the smallest values. Diagonal-freezing gave intermediate response. For field-frozen samples, $\chi_{diff}^{\max}$ and H_c increased with greater freezing field for parallel and diagonal orientations, but decreased for transverse orientation. However, increasing the freezing field from 10 to 15 mT/μ_0 did not produce a monotonic change in the response. The field-frozen sample response varied with the excitation field frequency (Fig. 6E,F), in agreement with previous investigations[3].

Here drive field frequencies were varied but amplitude was fixed at 50 mT/μ_0. $\chi_{diff}^{\max}$ varied slightly with frequency but with no clear trend, while coercivity increased monotonically with frequency. We note some variation in $\chi_{diff}^{\max}$ could have resulted from under-sampling due to the finite sample acquisition rate of our system (2M samples/s), which is exacerbated at higher frequencies.

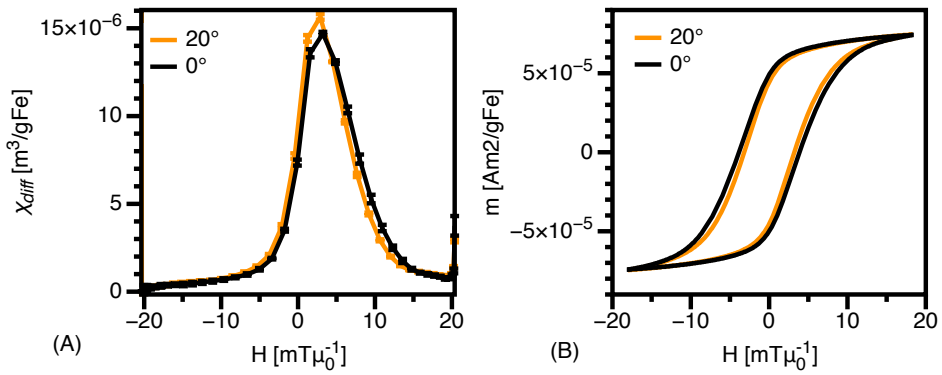

FIG. 8. MPS (26 kHz, 20 mT/μ_0) response of SPIOs in water at room temperature and 0 °C (liquid state). Error bars in A represent the standard deviation of three measurements.

The MPS response of liquid sample (dispersed in water) was measured at room temperature and 0°C. We note the slight variation in magnetic response due to temperature, particularly in the differential susceptibility (Fig. 8A). While the variation is close to the experimental error, slightly higher value of $\chi_{diff}^{\max}$ and reduced coercive field observed in the warmer sample may be expected in terms of the relaxation dynamics of the particles. When colder, magnetic reversal requires slightly greater energy, and therefore greater applied field, since thermal energy is reduced. These phenomena can be seen in Fig. 8, particularly in the differential susceptibility curve. The MPS responses of water-dispersed and liquid DMSO-dispersed samples were identical (data not shown).

A dilution series was prepared and frozen to observe how the freezing process affected sample magnetization dynamics. MPS analysis showed linear variation of signal intensity with the concentration for all freezing fields, as shown in Fig. 9, but with greater intensity per unit concentration at higher freezing fields. We found good agreement between simulations and experimental results and in particular show that the frozen particles act as if they are partially aligned by the field-freezing procedure. The linear change with concentration indicates that a combination of Brownian alignment and Néel rotations is possible in these

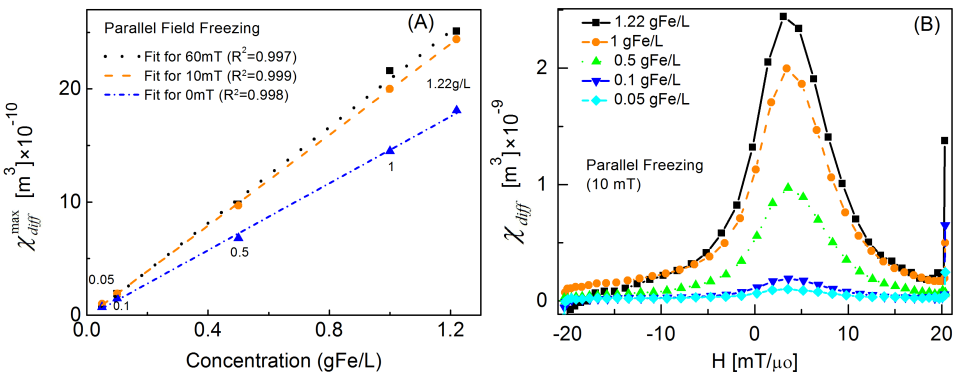

FIG. 9. $\chi^{\max}_{diff}$ data (at 26 kHz and 20 mT/μ_0) of different concentrations: (A) at different freezing fields, (B) at 10 mT/μ_0 parallel freezing.

particles, and to first order, the formation of chains can be ruled out. In Fig. 10, we show that the hysteresis loops change dramatically when frozen in the direction parallel to and perpendicular to the oscillating field that is applied. The simulations are identical except for an average reorientation of the easy axes. In each case, we simulate a 50% alignment in the direction of the static field in which the particles were frozen.

In Fig. 11 we show that the simulated hysteresis loops are quite different based on the phase of the suspending liquid, an effect much beyond simply changing the temperature, that has been previously studied in Cobalt nanoparticle solutions[33]. In particular, the melted sample shows an increase in the amount of saturation. This indicates potentially that the easy axes become slightly polarized in the direction of the oscillating field due to Brownian rotation. In this simulation, we account for partial (30%) alignment to the field. In the frozen sample however, the Brownian rotations should be restricted, and the fit is the most accurate without any alignment.

To show that increasing the strength of the applied static field affects the simulations in a similar way to the experiment, we simulated the hysteresis loops and the susceptibility of the magnetization at various applied field strengths, leading to various alignment percentages (Fig. 12). As the Brownian alignment increased, we saw the expected increase in the slope of the hysteresis as well as the delay in the peak of the slope caused by the anisotropy field parallel to the applied field. The susceptibility data were smoothed using a Gaussian window to avoid the artifacts that arise from taking a numerical derivative.

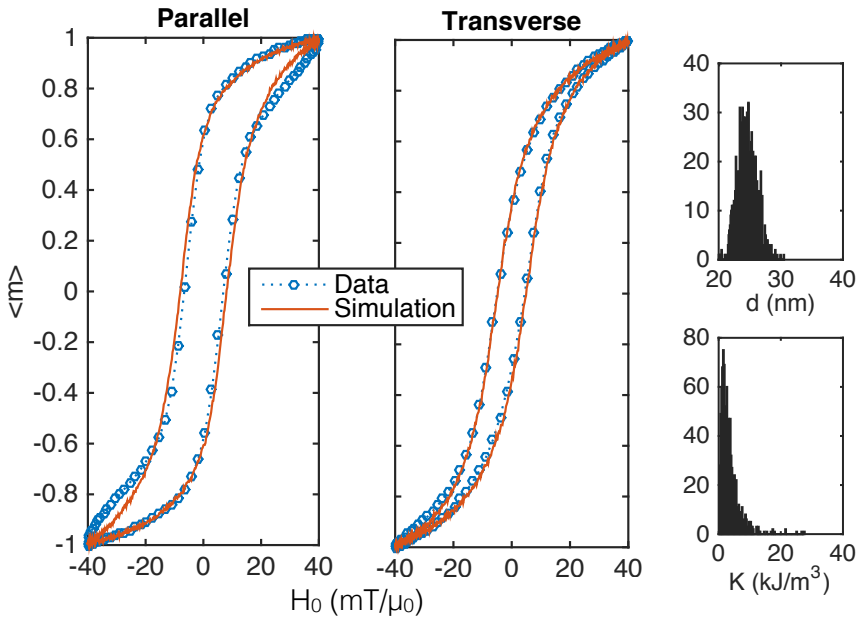

FIG. 10. Comparison between simulation and experiment for nanoparticles that were frozen while exposed to a 10 mT/μ_0 static field aligned parallel or perpendicular to the oscillating field. Then spectroscopy was performed using a 40 kHz, 20 mT/μ_0 field). The log-normal distributions of particle diameter and anisotropy constant are shown on the right by number in a representative 1000 particle sub-sample.

IV. DISCUSSION

The most significant result of this work was the observed difference in response between immobilized and liquid samples, indicating that both Néel relaxation and Brownian alignment mechanisms are possible in the liquid sample. In fact, for these particles, if the relaxation times are computed using the standard zero-field expressions for Néel and Brownian relaxation, they are of the same order of magnitude. Admittedly, these expressions are inappropriate to describe the dynamic response of particles forced to oscillate in a magnetic field, but if the relaxation times were many orders of magnitude different an adiabatic approximation would be reasonably made to ignore the slower mechanism[34]. Though both mechanisms seem to occur, the Néel mechanism appears to dominate, because a significant response can be measured from immobilized samples in which Brownian rotation should be quenched.

We hypothesized that variation between liquid and immobilized samples could result

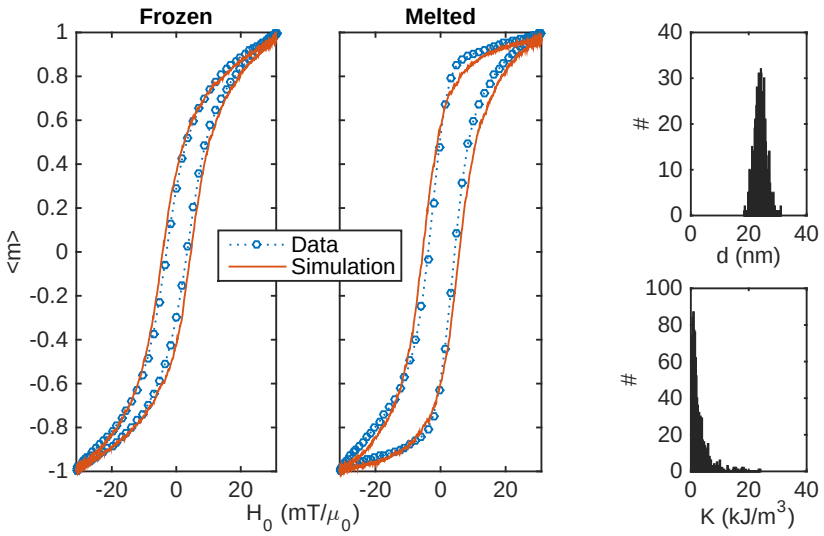

FIG. 11. Comparison between simulation and experiment for nanoparticles either in either a frozen or melted state. Spectroscopy was performed with a 26 kHz, 31 mT/μ_0 field. The log-normal distributions of particle diameter and anisotropy constant are shown on the right by number in a representative 1000 particle sub-sample.

from significant magnetic anisotropy in the nanoparticles. To investigate our hypothesis, we immobilized the SPIOs in DMSO, since the DMSO-nanoparticle suspension could be reproducibly frozen and melted to orient and re-orient the nanoparticles. Furthermore, DMSO stabilized the nanoparticles in solution and solid phases, with the nanoparticles displaying behaviors consistent with non-interacting particles (see Fig. 9 for the linear increase in magnetization with concentration).

To complement the experimental results, we simulated the dynamic particle magnetizations using a model based on the stochastic Landau-Lifshitz-Gilbert equation[20]. From the modeling, we saw almost identical magnetizations when the easy axes were partially aligned and a log-normal size distribution for the particle sizes and effective uniaxial anisotropy constant was included. We interpret the agreement with the effective uniaxial simulations to mean that an initial Brownian alignment causes one of the easy cubic axes to align with an applied static field, at which point the particles are frozen and fixed spatially. Subsequent Néel rotations depend on the direction of the alignment. The distribution of the anisotropy constant allows for several possible contributions to the anisotropy, and the form of the anisotropy energy depends on the constant and simply how much the magnetization

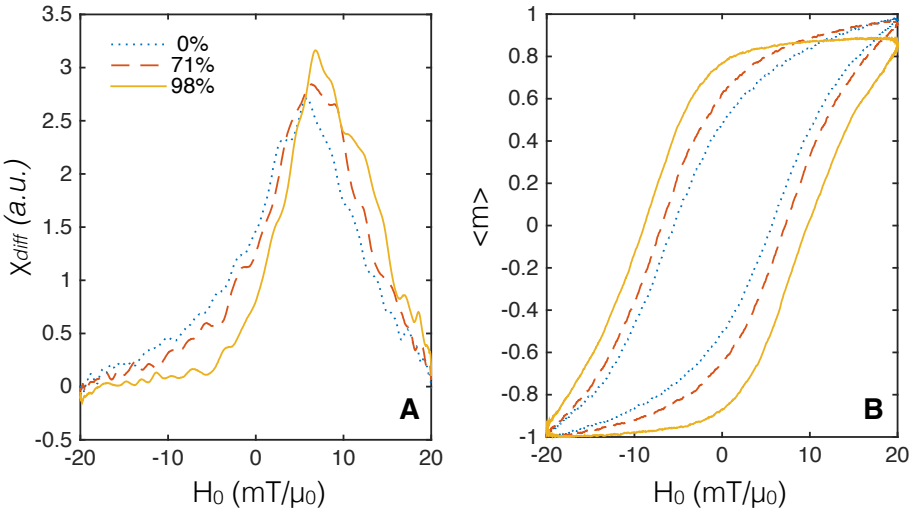

FIG. 12. Magnetizations were simulated using a 40 kHz, 20 mT/μ_0 field at room temperature to show how the (A) differential magnetic susceptibility in arbitrary units χ_{diff} (a.u.) and (B) hysteresis loops are effected by increasing the percentage of particles aligned in the direction of the applied field. The size and anisotropy distribution are identical to that in other simulations.

is aligned with the effective easy axis.

The parallel field-freezing alignment leads to higher slopes in the hysteresis curves (higher differential susceptibility χ_{diff}), and wider hysteresis loops (larger coercive fields H_c) than the diagonally or perpendicularly aligned particles. This behavior can be conceptualized by imagining a two state system where the energy barrier to magnetization reversal is the highest in when the magnetic field is aligned with the easy axis as in the parallel case.

The result that the fluid samples displayed steeper hysteresis curves is potentially more surprising and can be interpreted with simultaneous combinations of the Néel and Brown dynamics. It is possible to imagine that because the rotational timescales are comparable, the oscillating field might induce alignment of one of the easy crystalline axes. This effect is not extreme, the simulations only needed 30% alignment in some cases, but it is absolutely noticeable in the data (see for example Fig. 6A and Fig. 7).

The origin of the anisotropy is not fully clear. Magnetocrystalline anisotropy is expected for these particles and may be sufficient to explain the observed behavior, but only true

simultaneous *in situ* experiments such as high-resolution electron microscopy of liquid samples under applied fields could rule out the possibility of chaining. Moreover, it is hard to quantify the shape anisotropy of the particles from TEM imaging, though in the data of Fig. 2 it is clear they are quite monodisperse and any elongation is minor. Notwithstanding the fact that a TEM image renders a two-dimensional projection of a three-dimensional nanoparticle, a rough estimate of shape anisotropy of the particles was measured from TEM images using ImageJ. Each particle measured for size-determination was fit with an ellipse and the ratio of long axis to the short axis determined. The resulting histogram was fit with a log-normal distribution to determine the median aspect ratio (1.04 ± 0.03). This equates to a typical elongation of approximately 1 nm for the 26 nm diameter particles. We can estimate the anisotropy energy due to this minor elongation by considering the particles to be prolate ellipsoids of revolution with axes a, b, c, where $a > b = c$. In this case, the critical field for switching due to shape anisotropy is $H_k = M_s(N_b - N_a)$[35], where M_s is the saturation magnetization (263 kA/m), and N_a and N_b are the demagnetization factors along the a and b directions respectively. For the measured aspect ratio of 1.04 ± 0.03, H_k is about 5.2 mT/μ_0. For magnetocrystalline energy H_k would be expected of the order K/M_s, or 13 mT/μ_0, assuming $K = 3.4$ kJ/m^3; specifically, $H_k = 4K/3M_s$ for cubic systems, $H_k = 2K/M_s$ for uniaxial systems when the field is aligned anti-parallel to the moment, and $H_k = K/M_s$ for uniaxial systems when the field is aligned perpendicular to the moment, with the moment always assumed initially to be directed along an easy axis[36]. Since the magnetocrystalline anisotropy energy is greater, it should dominate in this sample, but shape anisotropy may contribute a slight uniaxial character. The magnetocrystalline and shape anisotropies would be similar with approximately 1.1 average particle aspect ratio.

In addition to alignment of individual particles, chain formation can be thought of as contributing to the effective anisotropy. Saville *et al.* showed that magnetite particles coated with 20 kDa PEG (with $M_s = 264$ kA/m, core diameter of 24 nm, and hydrodynamic diameter of 170 nm) formed chains averaging 3 μm long were observed after applying a steady field of 270 mT/μ_0 for 30 s[37]. Chain formation may have occurred during the field-freezing experiments reported here, although it is less likely to have affected MPS of liquid samples, since only weak oscillating fields were applied and our MPS has a 50% duty cycle (the field is switched off for 0.5 s every 1 s).

The magnetically optimized, monodisperse SPIOs used in this study showed highly non-

linear behavior, producing a sharp magnetization response useful for sensing and imaging applications that use magnetic induction, such as MPI. With uniformly sized magnetic cores and well-defined hydrodynamic size, the samples were also ideal for studies of how particles behavior responds to variations in the drive field, since variations in response can be assumed to come from uniform changes in the response of each particle, rather than from multiple fractions of varying size, as in clustered-core particles like Resovist.

V. CONCLUSIONS

This work arose from the observation that immobilized (frozen) SPIOs displayed distinctly different rotational dynamics than the same particles in a liquid state. This phenomenon was well beyond the respective change in the relaxation time purely due to the temperature. It was previously expected that the particles would reorient their magnetic moment internally, with the Néel mechanism, and thus the local environment (e.g., the phase of the solution) should have had no impact. The large change in the dynamics is equivalent to an effective uniaxial anisotropy that could be due to small chain formations or local reorientation of the particles themselves. For spherical nanoparticles with cubic symmetry, only a slight physical rotation, referred to here as Brownian alignment, is required to align one of the magnetocrystalline easy axes along the applied field direction. The dynamics of the particles in a randomly frozen state were still different from the liquid state dynamics. This indicates that even while Néel oscillations occur, a general alignment through Brownian rotation is possible in the liquid sample. All of these dynamical behaviors could be replicated using Langevin equation simulations. The partial alignment of the easy axes could be incorporated into the model through the effective field of the Landau-Lifshitz-Gilbert equation. We also found that while the magnetic particles are predicted to have cubic anisotropy, a single effective axis with a large distribution over the anisotropy constant is adequate to account for the observable dynamical effects.

In the future, it appears wise to specifically characterize any magnetic particles used in dynamical applications, as typical equilibrium calculations of relaxation times alone are inadequate predictors of rotational mechanisms. We have demonstrated that an initial Brownian alignment, leading to an effective uniaxial anisotropy, plays an important role for magnetic nanoparticles conventionally thought to only rotate with the Néel mechanism. This

result has far reaching implications for emerging biomedical technologies such as magnetic particle imaging (MPI).

ACKNOWLEDGMENTS

This work was supported by NIH grants 2R42EB013520-02A1, a UW/CGF commercialization grant and a Commercialization Fellowship (RMF). Dr Saqlain Shah, is grateful to Higher Education Commission (HEC), Government of Pakistan, for financial assistance.

REFERENCES

[1]Kannan M Krishnan. Biomedical nanomagnetics: a spin through possibilities in imaging, diagnostics, and therapy. *Magnetics, IEEE Transactions on*, 46(7):2523–2558, 2010.

[2]Bernhard Gleich and Jürgen Weizenecker. Tomographic imaging using the nonlinear response of magnetic particles. *Nature*, 435(7046):1214–1217, 2005.

[3]Saqlain A Shah, RM Ferguson, and KM Krishnan. Slew-rate dependence of tracer magnetization response in magnetic particle imaging. *Journal of Applied Physics*, 116(16):163910, 2014.

[4]R Ferguson, A Khandhar, E Saritas, L Croft, P Goodwill, A Halkola, J Borgert, J Rahmer, S Conolly, and K Krishnan. Magnetic particle imaging with tailored iron oxide nanoparticle tracers. *IEEE Transactions on Medical Imaging*, 2014.

[5]M Visscher, S Waanders, HJG Krooshoop, and B ten Haken. Selective detection of magnetic nanoparticles in biomedical applications using differential magnetometry. *Journal of magnetism and magnetic materials*, 365:31–39, 2014.

[6]Adam M Rauwerdink, Andrew J Giustini, and John B Weaver. Simultaneous quantification of multiple magnetic nanoparticles. *Nanotechnology*, 21(45):455101, 2010.

[7]J Rahmer, A Halkola, B Gleich, I Schmale, and J Borgert. First experimental evidence of the feasibility of multi-color magnetic particle imaging. *Physics in medicine and biology*, 60(5):1775, 2015.

[8]Julian Carrey, Boubker Mehdaoui, and Marc Respaud. Simple models for dynamic hysteresis loop calculations of magnetic single-domain nanoparticles: Application to magnetic hyperthermia optimization. *Journal of Applied Physics*, 109(8):083921, 2011.

[9]L Néel. Théorie du traînage magnétique des ferromagnétiques en grains fins avec applications aux terres cuites. *Annals Géophysics*, 5(2):99–136, 1949.

[10]Albert Einstein. *Investigations on the Theory of the Brownian Movement*. Courier Corporation, 1956.

[11]C Haase and U Nowak. Role of dipole-dipole interactions for hyperthermia heating of magnetic nanoparticle ensembles. *Physical Review B*, 85(4):045435, 2012.

[12]Irene Andreu, Eva Natividad, Laura Solozábal, and Olivier Roubeau. Nano-objects for addressing the control of nanoparticle arrangement and performance in magnetic hyperthermia. *ACS nano*, 9(2):1408–1419, 2015.

[13]Patricia de la Presa, Yurena Luengo, Victor Velasco, MP Morales, M Iglesias, Sabino Veintemillas-Verdaguer, Patricia Crespo, and Antonio Hernando. Particle interactions in liquid magnetic colloids by zero field cooled measurements: Effects on heating efficiency. *The Journal of Physical Chemistry C*, 119(20):11022–11030, 2015.

[14]RW Chantrell, J Popplewell, and Stuart Charles. Measurements of particle size distribution parameters in ferrofluids. *Magnetics, IEEE Transactions on*, 14(5):975–977, 1978.

[15]R Matthew Ferguson, Amit P Khandhar, and Kannan M Krishnan. Tracer design for magnetic particle imaging. *Journal of applied physics*, 111(7):07B318, 2012.

[16]Daniel B Reeves and John B Weaver. Nonlinear simulations to optimize magnetic nanoparticle hyperthermia. *Applied Physics Letters*, 104(10):102403, 2014.

[17]NA Usov and Yu B Grebenshchikov. Hysteresis loops of an assembly of superparamagnetic nanoparticles with uniaxial anisotropy. *Journal of Applied Physics*, 106(2):023917, 2009.

[18]Isaak D Mayergoyz, Giorgio Bertotti, and Claudio Serpico. *Nonlinear magnetization dynamics in nanosystems*. Elsevier, 2009.

[19]Jürgen Weizenecker, Bernhard Gleich, Jürgen Rahmer, and Jörn Borgert. Micro-magnetic simulation study on the magnetic particle imaging performance of anisotropic monodomain particles. *Physics in Medicine and Biology*, 57(22):7317, 2012.

[20]William Fuller Brown Jr. Thermal fluctuations of a single-domain particle. *Journal of Applied Physics*, 34(4):1319–1320, 1963.

[21]KM Krishnan, AB Pakhomov, Y Bao, P Blomqvist, Y Chun, M Gonzales, K Griffin, X Ji, and BK Roberts. Nanomagnetism and spin electronics: materials, microstructure and novel properties. *Journal of Materials Science*, 41(3):793–815, 2006.

[22]Matthieu Jamet, Wolfgang Wernsdorfer, Christophe Thirion, Veronique Dupuis, Patrice Mélinon, Alain Pérez, and Dominique Mailly. Magnetic anisotropy in single clusters. *Physical Review B*, 69(2):024401, 2004.

[23]Alexandre Tamion, Matthias Hillenkamp, Florent Tournus, Edgar Bonet, and Veronique Dupuis. Accurate determination of the magnetic anisotropy in cluster-assembled nanostructures. *Applied Physics Letters*, 95(6):062503, 2009.

[24]MI Shliomis and VI Stepanov. Theory of the dynamic susceptibility of magnetic fluids. *Advances in Chemical Physics*, 87(1):32, 1994.

[25]WT Coffey, PJ Cregg, and YUP Kalmykov. On the theory of debye and néel relaxation of single domain ferromagnetic particles. *Advances in Chemical Physics, Volume 83*, pages 263–464, 2007.

[26]Crispin W Gardiner et al. *Handbook of stochastic methods*, volume 4. Springer Berlin, 1985.

[27]Peter E Kloeden and Eckhard Platen. *Numerical solution of stochastic differential equations*, volume 23. Springer, 1992.

[28]Ch Kittel and Elihu Abrahams. Relaxation process in ferromagnetism. *Reviews of Modern Physics*, 25(1):233, 1953.

[29]Thomas L Gilbert. A phenomenological theory of damping in ferromagnetic materials. *Magnetics, IEEE Transactions on*, 40(6):3443–3449, 2004.

[30]Gabriel T Landi. Influence of the magnetization damping on dynamic hysteresis loops in single domain particles. *Journal of Applied Physics*, 111(4):043901, 2012.

[31]Ning-Ning Song, Hai-Tao Yang, Hao-Liang Liu, Xiao Ren, Hao-Feng Ding, Xiang-Qun Zhang, and Zhao-Hua Cheng. Exceeding natural resonance frequency limit of monodisperse Fe_3O_4 nanoparticles via superparamagnetic relaxation. *Scientific Reports*, 3, 2013.

[32]Frank Ludwig, Hilke Remmer, Christian Kuhlmann, Thilo Wawrzik, Hamed Arami, R Mathew Ferguson, and Kannan M Krishnan. Self-consistent magnetic properties of magnetite tracers optimized for magnetic particle imaging measured by ac susceptometry, magnetorelaxometry and magnetic particle spectroscopy. *Journal of Magnetism and Magnetic Materials*, 360:169–173, 2014.

[33]Tianlong Wen, Wenkel Liang, and Kannan M Krishnan. Coupling of blocking and melting in cobalt ferrofluids. *Journal of Applied Physics*, 107(9):09B501, 2010.

[34]Daniel B Reeves and John B Weaver. Comparisons of characteristic timescales and approximate models for brownian magnetic nanoparticle rotations. *Journal of applied physics*, 117(23):233905, 2015.

[35]Edmund C Stoner and EP Wohlfarth. A mechanism of magnetic hysteresis in heterogeneous alloys. *Philosophical Transactions of the Royal Society of London A: Mathematical, Physical and Engineering Sciences*, 240(826):599–642, 1948.

[36]Sōshin Chikazumi. *Physics of magnetism*. Wiley, 1964.

[37]Steven L Saville, Robert C Woodward, Michael J House, Alexander Tokarev, Jacob Hammers, Bin Qi, Jeremy Shaw, Martin Saunders, Rahi R Varsani, Tim G St Pierre, et al. The effect of magnetically induced linear aggregates on proton transverse relaxation rates of aqueous suspensions of polymer coated magnetic nanoparticles. *Nanoscale*, 5(5):2152–2163, 2013.